

# Enhanced quantum state transfer and Bell-state generation over long-range multimode interconnects via superadiabatic transitionless driving

Moein Malekakhlagh<sup>1,\*</sup>, Timothy Phung,<sup>2</sup> Daniel Puzzuoli,<sup>3</sup> Kentaro Heya,<sup>1</sup> Neereja Sundaresan,<sup>1</sup> and Jason Orcutt<sup>1</sup>

<sup>1</sup>IBM Quantum, Thomas J. Watson Research Center, 1101 Kitchawan Road, Yorktown Heights, New York 10598, USA

<sup>2</sup>IBM Quantum, Almaden Research Center, 650 Harry Road, San Jose, California 95120, USA

<sup>3</sup>IBM Quantum, IBM Canada, 750 West Pender Street, Vancouver, British Columbia V6C 2T8, Canada



(Received 27 January 2024; revised 1 May 2024; accepted 9 July 2024; published 2 August 2024)

Achieving high-fidelity direct two-qubit gates over meter-scale quantum interconnects is challenging, in part due to the multimode nature of such systems. One alternative scheme is to combine local operations with remote quantum state transfer or remote entanglement. Here, we theoretically study quantum state transfer and entanglement generation for two distant qubits, equipped with tunable interactions, over a common multimode interconnect. We model the performance of the superadiabatic transitionless driving (SATD) protocol for adiabatic passage and demonstrate various favorable improvements over the standard method. In particular, by suppressing leakage to a select (resonant) interconnect mode, SATD breaks the speed-limit relation imposed by the qubit-interconnect interaction  $g$ , where instead the operation time is limited by leakage to the adjacent modes, i.e., the free spectral range  $\Delta_c$  of the interconnect, allowing for fast operations even with weak  $g$ . Furthermore, we identify a multimode error mechanism for Bell-state generation using such adiabatic protocols, in which the even/odd modal dependence of qubit-interconnect interaction breaks down the dark-state symmetry, leading to detrimental adiabatic overlap with the odd modes growing as  $(g/\Delta_c)^2$ . Therefore, adopting a weak coupling, imposed by a multimode interconnect, SATD provides a significant improvement in terms of operation speed and consequently sensitivity to incoherent error.

DOI: 10.1103/PhysRevApplied.22.024006

## I. INTRODUCTION

Modular design of quantum computers [1–3] reduces the complexity of wiring and control—as well as the power requirements for cryogenic cooling—of the underlying quantum processing units (QPUs); as such, it is the path forward for the required scaling [4–6] toward quantum error correction [7–11]. For superconducting qubits, this vision necessitates developing interconnects at various levels of modularity [3], such as dense short-range interconnects [12,13] to extend the effective size of QPUs, and sparse meter-range interconnects to enable parallelization of multiple QPUs within a dilution fridge. The short-range interconnect length is comparable to the distance between the qubits within a single chip and the system thus behaves effectively as a single-mode system. While standard two-qubit gates could potentially work across a short interconnect, the multimode nature of long-range interconnects makes *direct* two-qubit gates more difficult. Two alternatives are to use the interconnect to perform state

transfer or to generate remote entanglement such as a Bell state. In conjunction with local operations and classical communication, either of these operations can be used as a resource to implement indirect remote two-qubit gates [14–16].

The past few years have seen a recent surge into numerous superconducting circuit realizations for remote entanglement generation and quantum state transfer [18–29]. These protocols can be broadly categorized as either employing time-symmetric emission and capture [30,31] of itinerant photons [18–20,22,23,27–29] or using qubit interactions with the standing-wave modes of meter-scale interconnects [21,22,24,25,29]. Among protocols based on standing-wave modes, stimulated Raman adiabatic passage (STIRAP) [32–34] achieves better fidelity [24] compared with a qubit-interconnect-qubit direct excitation exchange, also referred to as the relay protocol [22], by protection against interconnect loss.

In STIRAP [32–34], we evolve the dark eigenstate of a Lambda system adiabatically toward a desired target state, which is applicable to quantum state transfer and entanglement generation. One advantage of this approach is the

\*Contact author: moein.malekakhlagh@ibm.com

suppression of potential relaxation through the intermediate lossy interconnect. The operation speed is, however, limited by leakage to the bright lossy eigenstates, whose transition frequency is set by the coupling strength. Transitionless driving methods [35–39] cancel out nonadiabatic transitions *exactly* via a modified control Hamiltonian; this is similar in spirit to the *perturbative* derivative-removal-by-adiabatic-gate technique [40–43]. One potential practical drawback, however, is the need for a control knob not accessible by the original Hamiltonian. Superadiabatic transitionless driving (SATD) [17,44–47] redefines the evolution path, connecting the original source and target states such that in the dressed frame, the nonadiabatic transitions are canceled out exactly without the need for additional control knobs. SATD solutions for STIRAP have also been generalized to single-qubit tripod gates [48,49] and more recently to two-qubit gates [50] for fluxonium qubits [51].

In this paper, we model the performance improvements of the SATD protocol against STIRAP and promote its use for quantum state transfer and Bell-state generation in a *meter-range multimode* interconnect setting. By removing leakage to the resonant interconnect mode, the operation speed for SATD is no longer limited by the qubit-cable coupling  $g$  but is determined by the free spectral range (FSR) of the interconnect  $\Delta_c$ , leading to a significant speedup as well as a robustness to variation in  $g$  compared with STIRAP. We show that the single-mode SATD solutions work reasonably well for a multimode interconnect with sufficiently large FSR ( $\Delta_c \gg g$ ), and we quantify the deviations from expected behavior due to multimode effects. In particular, we find that the even-odd mode dependence of the interaction breaks the dark-state symmetry, which is in principle detrimental to such dark-state-based adiabatic protocols. This impacts the Bell-state generation more by an adiabatic overlap error proportional to  $(g/\Delta_c)^2$ , and this can be mitigated only via a weaker  $g$ . This requirement for weaker  $g$  due to multimode effects, along with the  $g$  robustness of SATD, makes its application very advantageous, especially for Bell-state generation. Furthermore, we observe improvements by SATD in suppressing the incoherent error due to qubit relaxation, pure dephasing, and the interconnect quality factor.

The remainder of this paper is organized as follows. Section II describes the system under consideration, with two quantum modules connected via a multimode interconnect, and a Lindblad model is introduced for our analytical and numerical analyses. In Sec. III, we revisit the ideal single-mode STIRAP protocol, which is used for quantum state transfer and entanglement generation, and we discuss potential detrimental multimode sources of error. In Sec. IV, we present extensive simulations investigating the numerous advantages of SATD compared with regular STIRAP in such a multimode context. We further assess the performance of indirect two-qubit gates

achieved by combining quantum state transfer and remote entanglement with local operations. Appendix A discusses the details of our Lindblad model and simulations and provides a numerical convergence test. Appendices B and C review the single-mode STIRAP and complications that arise due to the use of a multimode interconnect, respectively. In Appendix D, we review the derivation of SATD solutions for single-mode STIRAP following Ref. [17].

## II. SYSTEM AND MODEL

We consider a system consisting of two tunable-frequency qubits that have tunable interactions via a common meter-range multimode interconnect, as depicted in Fig. 1(a). The standard motivation for such a setup is to perform remote quantum operations between two modules (chips) connected via a long interconnect such as a coaxial cable. This can, however, also be relevant to on-chip transmission lines between distant qubits [52]. Notable experimental studies have employed tunable grounded transmon qubits with tunable rf superconducting quantum interference device couplers [53–55] connected via an on-chip transmission line [24] or a cable [29].

We characterize the performance of the STIRAP and SATD protocols for quantum state transfer and Bell-state generation via a Lindblad simulation that accounts for qubit relaxation ( $T_1$ ), pure dephasing ( $T_{2\phi}$ ), and cable relaxation ( $\kappa_n$ ):

$$\begin{aligned} \dot{\hat{\rho}}_s(t) = & -i[\hat{H}_s(t), \hat{\rho}_s(t)] + \sum_{q=a,b} \frac{1}{T_{1q}} \mathcal{D}[\hat{q}] \hat{\rho}_s(t) \\ & + \sum_{q=a,b} \frac{2}{T_{2\phi,q}} \mathcal{D}[\hat{q}^\dagger \hat{q}] \hat{\rho}_s(t) + \sum_n \kappa_n \mathcal{D}[\hat{c}_n] \hat{\rho}_s(t), \quad (1) \end{aligned}$$

where  $\hat{\rho}_s(t)$  is the system density matrix and  $\mathcal{D}[\hat{C}] \hat{\rho}_s \equiv \hat{C} \hat{\rho}_s \hat{C}^\dagger - (1/2)\{\hat{C}^\dagger \hat{C}, \hat{\rho}_s\}$  is the dissipator for the collapse operator  $\hat{C}$ . We model the qubits as weakly anharmonic and the interconnect as a collection of harmonic quantum oscillators, with time-dependent (controllable) qubit-interconnect interaction as

$$\begin{aligned} \hat{H}_s(t) = & \sum_{q=a,b} \left[ \omega_q(t) \hat{q}^\dagger \hat{q} + \frac{\alpha_q}{2} \hat{q}^\dagger \hat{q}^\dagger \hat{q} \hat{q} \right] + \sum_{n-n_c=-N}^N \omega_n \hat{c}_n^\dagger \hat{c}_n \\ & + \sum_{n-n_c=-N}^N g_{an}(t) (\hat{a} \hat{c}_n^\dagger + \hat{a}^\dagger \hat{c}_n) \\ & + \sum_{n-n_c=-N}^N g_{bn}(t) (-1)^n (\hat{b} \hat{c}_n^\dagger + \hat{b}^\dagger \hat{c}_n), \quad (2) \end{aligned}$$

where  $\omega_q(t)$ ,  $\alpha_q$ ,  $\omega_n = \omega_{n_c} + n\Delta_c$ , and  $g_{qn}(t)$  are the qubit frequency, anharmonicity, evenly spaced  $n$ th mode frequency with FSR  $\Delta_c$ , and qubit-interconnect interaction

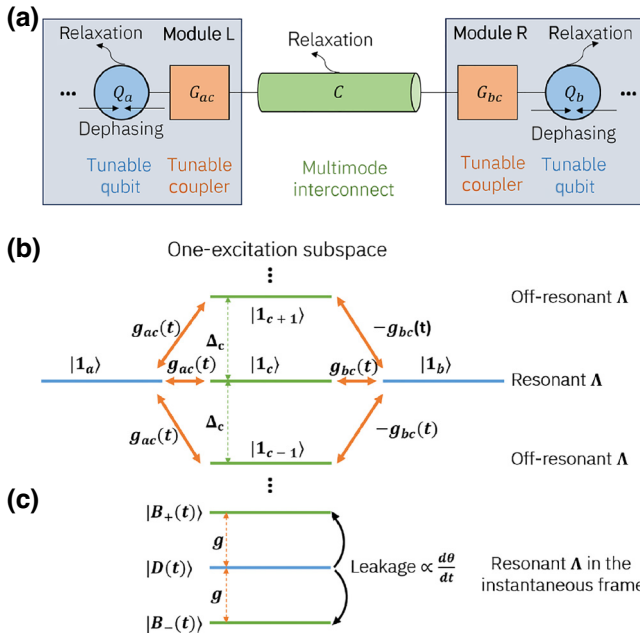


FIG. 1. System schematics and energy level diagram. (a) Two quantum modules each with tunable-frequency qubits and tunable coupling to a shared meter-range multimode interconnect. We account for incoherent error due to qubit/interconnect relaxation and qubit pure dephasing. (b) Energy-level diagram in the one-excitation subspace. Bringing the qubits into resonance with a center mode forms a resonant Lambda system. There are, however, off-resonant Lambda systems formed by the adjacent interconnect modes with mode-dependent interaction signs that are detuned by an FSR  $\Delta_c$  corresponding to a meter in length. (c) The resonant Lambda system in the instantaneous frame forms a dark eigenstate; using this, one can implement STIRAP and its enhanced version SATD [17], in which we actively cancel out the dark-bright leakage transition. The leakage is proportional to the derivative of the STIRAP mixing angle  $\theta(t) \equiv \arctan(g_{ac}(t)/g_{bc}(t))$  (Appendices B and D).

rates for  $q = a, b$ , respectively;  $n_c$  is the center mode index and  $N$  is the additional modes kept on each side. The interconnect length  $l_c$  is related to its FSR as  $\Delta_c \equiv v_p/(2l_c)$ , with  $v_p$  as the phase velocity, which we take to be about a meter long in our analysis. In writing the Hamiltonian (2), we have made certain approximations, motivated by the physics of multimode interconnects (see Appendix A), similar to in Ref. [24]. An important feature of the Hamiltonian (2) is the even-odd mode-dependent relative sign for the qubit-interconnect interaction, which accounts for the distinct spatial profile of even and odd interconnect modes [24].

While the above Hamiltonian description is motivated by a superconducting architecture consisting of frequency-tunable transmon qubits connected by tunable couplers to a superconducting coaxial cable, other physical hardware implementations can have similar Hamiltonian descriptions. Examples of such systems include optical cavity-QED systems connected by photonic waveguides

[56,57], or solid-state systems connected via photonic crystal nanocavities [58,59]. In each case, the frequency mode spacing between the modes (FSR) is determined by the length of the interconnect, which is typically a meter long. Thus, the analysis and characterization we now present can also be applied to examine these physical implementations.

### III. STIRAP VIA A MULTIMODE INTERCONNECT

STIRAP is a protocol for adiabatic transfer of population in a Lambda system—i.e., between two quantum states coupled through a common intermediate state—via temporal control of the interactions [Fig. 1(b)]. Under the single-mode (ideal) case, the Hamiltonian reads

$$\hat{H}_{\text{STIRAP}}(t) = \begin{bmatrix} 0 & g_{ac}(t) & 0 \\ g_{ac}(t) & 0 & g_{bc}(t) \\ 0 & g_{bc}(t) & 0 \end{bmatrix}, \quad (3)$$

where we assume that all levels are resonant. This resonant Lambda system has a dark eigenstate

$$|D(t)\rangle \equiv \cos \theta(t) |1_a 0_c 0_b\rangle - \sin \theta(t) |0_a 0_c 1_b\rangle \quad (4)$$

and two bright eigenstates

$$|B_{\pm}(t)\rangle \equiv \frac{1}{\sqrt{2}} [\sin \theta(t) |1_a 0_c 0_b\rangle \pm |0_a 1_c 0_b\rangle + \cos \theta(t) |0_a 0_c 1_b\rangle], \quad (5)$$

with the mixing angle defined as  $\tan \theta(t) \equiv g_{ac}(t)/g_{bc}(t)$ .

The dark eigenstate, having no overlap with the intermediate (possibly) lossy interconnect state, therefore allows for an adiabatic quantum state transfer by arbitrarily evolving the mixing angle  $\theta(t)$ . Common choices for the controls are  $g_{ac}(t) = g \sin \theta(t)$  and  $g_{bc}(t) = g \cos \theta(t)$ , with  $\theta(t) = (t/\tau_p)\theta_p$  for  $t \in [0, \tau_p]$ . For instance, sweeping  $\theta(t)$  from 0 to  $\pi/2$  or  $\pi/4$  should ideally implement  $|1_a 0_c 0_b\rangle \rightarrow -|0_a 0_c 1_b\rangle$  (full state transfer), or  $|1_a 0_c 0_b\rangle \rightarrow 1/\sqrt{2}(|1_a 0_c 0_b\rangle - |0_a 0_c 1_b\rangle)$  (Bell state), respectively; note, however, that unwanted nonadiabatic  $|D(t)\rangle \rightarrow |B_{\pm}(t)\rangle$  transitions, whose probabilities grow with  $\dot{\theta}(t)$ , impose a limit on the STIRAP speed [Fig. 1(c) and Appendix B].

For a multimode interconnect, with the interaction  $g$  comparable to the FSR  $\Delta_c$ , the adjacent modes detrimentally impact the fidelity of STIRAP by (i) breaking the dark-symmetry condition, (ii) introducing additional leakage, and (iii) additional decay channels. Regarding item (i), each adjacent mode forms an effective off-resonant Lambda system with the qubits [Fig. 1(b)]. Our extended multimode STIRAP analysis suggests that for a hypothetical interconnect with same-sign interactions the Hamiltonian supports the original dark eigenstate, while

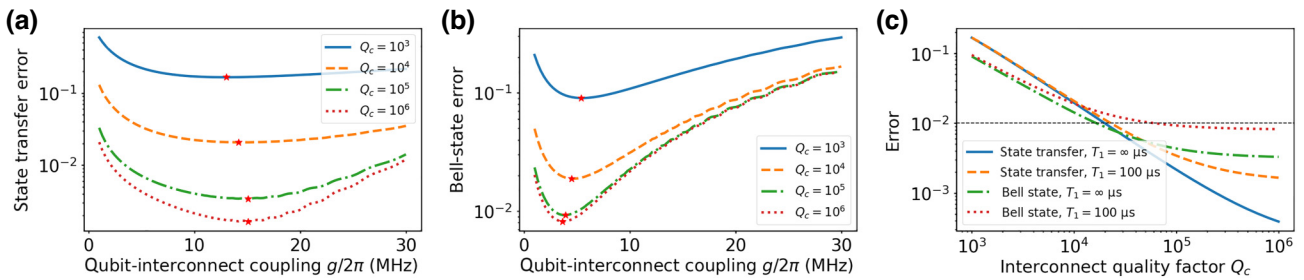


FIG. 2. Characterization of STIRAP performance for state transfer and Bell-state generation via a multimode interconnect: (a) state transfer error and (b) Bell-state error, as a function of qubit-interconnect coupling  $g$  for various interconnect quality factors  $Q_c \in [10^3, 10^6]$  (same for all modes). We included five interconnect modes, with  $\Delta_c/2\pi = 100$  MHz, where the center mode is resonant with the qubits (see Appendix A for a convergence test). Qubit relaxation is set to  $T_{1,a} = T_{1,b} = 100$   $\mu$ s. Here, for each value of  $g$ , the operation time is set to minimize dark  $\rightarrow$  bright leakage as  $g\tau_p = 4\pi$  [24]. STIRAP angles for state transfer and Bell-state generation are  $\theta_p = \pi/2$  and  $\theta_p = \pi/4$ , respectively. Note that optimal couplings for state transfer and Bell-state generation (red stars) are distinct and are found as approximately  $g/2\pi \approx 15$  and  $4$  MHz, respectively. (c) State transfer and Bell-state generation error as a function of  $Q_c$  using the optimal  $g$  in (a),(b).

for the physical case of mode-dependent interactions, one instead finds a pseudo dark eigenstate having a nonzero overlap  $|[g(t)/\Delta_c] \sin[2\theta(t)]|$  with the one-excitation subspace of the odd (opposite-sign) modes (Appendix C). Such an adiabatic error vanishes for quantum state transfer with  $\theta(\tau_p) = \pi/2$  but is maximized for Bell state generation with  $\theta(\tau_p) = \pi/4$  requiring a weaker  $g$  for better fidelity.

Figure 2 characterizes the performance of STIRAP in such a multimode context, where we numerically simulate the Lindblad equations [Eqs. (1) and (2)] with five interconnect modes evenly spaced about the qubit frequency for the common sine/cosine STIRAP controls and initial pure state  $\hat{\rho}_s(0) \equiv |1_a 0_c 0_b\rangle \langle 1_a 0_c 0_b|$ . We define the error

$$E \equiv 1 - \text{Tr}\{\hat{\rho}_s(\tau_p) |\psi_{\text{id}}\rangle \langle \psi_{\text{id}}|\} \quad (6)$$

in terms of the overlap of the final density matrix with the ideal target states for state transfer and Bell-state generation as  $|\psi_{\text{id}}\rangle = |0_a 0_c 1_b\rangle$  and  $|\psi_{\text{id}}\rangle = (1/\sqrt{2})(|1_a 0_c 0_b\rangle - |0_a 0_c 1_b\rangle)$ , respectively. Figures 2(a) and 2(b) show the corresponding error as a function of  $g$  for a fixed FSR of  $\Delta_c/2\pi = 100$  MHz and various interconnect quality factors; here, we observe distinct approximate optimal  $g/\Delta_c$  ratios of 15% and 4% for state transfer and Bell-state generation, respectively, at  $Q_c = 10^5$  and  $T_{1a} = T_{1b} = 100$   $\mu$ s. The optimal couplings are a balance between more leakage to the neighboring modes at stronger  $g$  (faster operation) and more incoherent error at weaker  $g$  (slower operation). The Bell-state generation also suffers from a nonzero *adiabatic* overlap with the odd interconnect modes due to dark-state symmetry breakdown (Appendix C and Sec. IV B). Using the optimal couplings in Fig. 2(c), we find that to reach subpercent error, the interconnect  $Q_c$

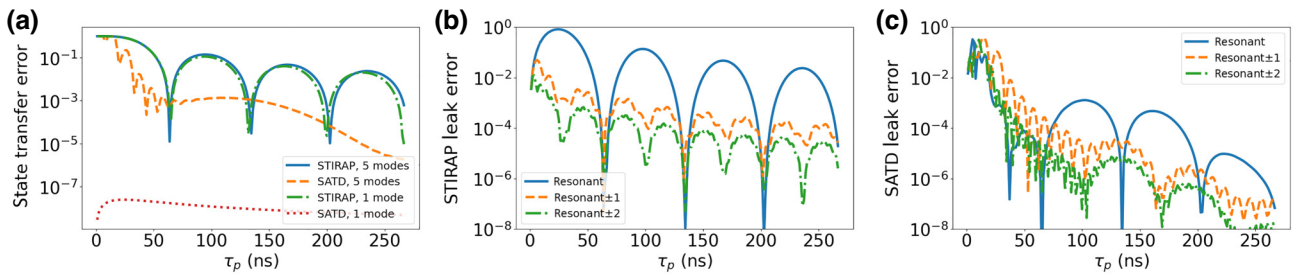


FIG. 3. Comparison of the performance and leakage breakdown for quantum state transfer of STIRAP versus SATD: (a) state-transfer error considering one (ideal) and five interconnect modes; (b),(c) final leakage, i.e., at  $t = \tau_p$ , to the interconnect modes for the five-mode STIRAP and SATD simulations, respectively. The result is found by numerical simulation of Eqs. (1) and (2), where here the incoherent relaxation and dephasing channels are turned off. Qubit-interconnect interactions and FSR are set to  $g/2\pi = 15$  (optimal choice from Fig. 2) and  $\Delta_c/2\pi = 100$  MHz, respectively. Leakage to interconnect modes that are symmetrically above and below the center frequency is identical and is shown via a single curve.

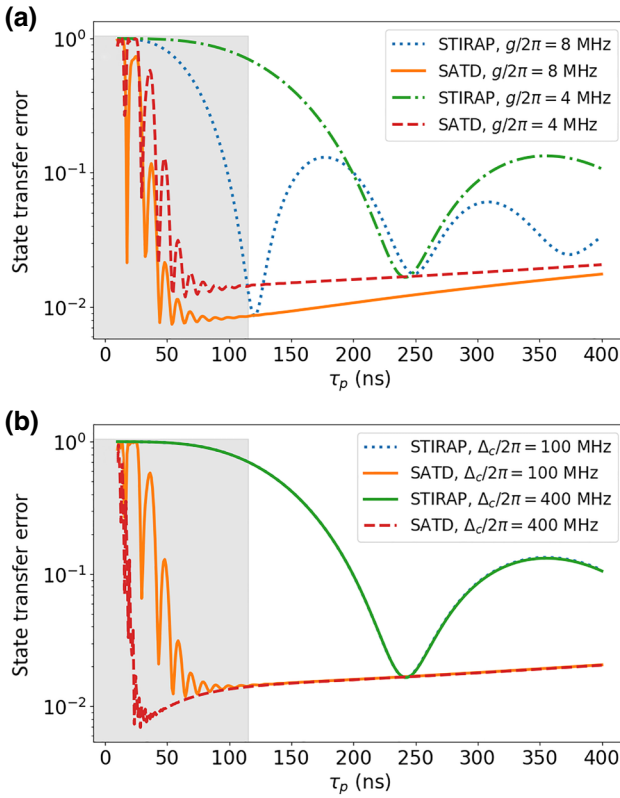


FIG. 4. Robustness of SATD with respect to qubit-interconnect interaction  $g$ : state transfer error as a function of  $\tau_p$  for (a) two weak values of  $g/2\pi = 8$  and  $4$  MHz; (b) two values of FSR  $\Delta_c/2\pi = 100$  and  $400$  MHz and fixed  $g/2\pi = 4$  MHz. Other parameters are set as  $T_{1,a} = T_{1,b} = 100$   $\mu$ s,  $T_{2\phi,a} = T_{2\phi,b} = 10$   $\mu$ s,  $Q_c = 10^5$ . The two STIRAP curves in panel (b) lie on top. The shaded gray area marks the parameter region for which the derivative corrections in SATD require a larger-than- $g$  maximum pulse amplitude for  $g/2\pi = 4$  MHz (Appendix D).

must approximately exceed  $2.2 \times 10^4$  and  $6.5 \times 10^4$  for state transfer and Bell-state generation, respectively.

#### IV. IMPROVED STIRAP VIA SUPERADIABATIC TRANSITIONLESS DRIVING

Transitionless driving is a control technique for canceling out nonadiabatic transitions via a corrected control Hamiltonian [35–38]. In an ideal case, from the hardware perspective, the correction can be simply implemented via a modification of the original control pulses. The superadiabatic aspect refers to implementing the cancellation in a dressed frame, i.e., effectively evolving the initial state in a modified path in the Hilbert space toward the target state. The standard single-mode STIRAP problem allows for a family of exact SATD solutions [17]. A commonly employed SATD solution dresses the evolution path along the spin-1  $\hat{M}_x$  operator, yielding the explicit results

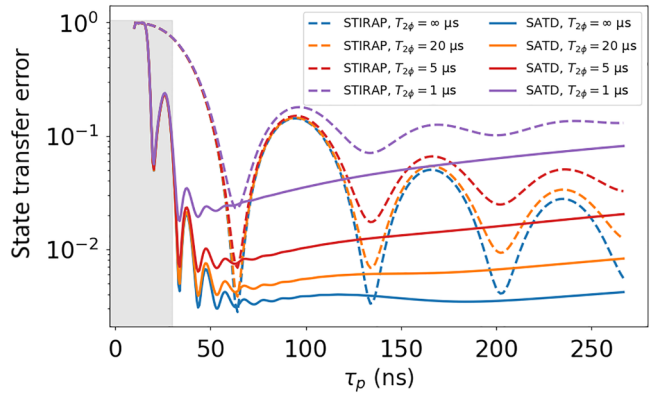


FIG. 5. Dependence of state transfer error on pure dephasing: comparing STIRAP and SATD as a function of  $\tau_p$  for various dephasing times  $T_{2\phi,a} = T_{2\phi,b} \in \{\infty, 20, 5, 1\}$   $\mu$ s. Other parameters are set as  $T_{1,a} = T_{1,b} = 100$   $\mu$ s,  $Q_c = 10^5$ ,  $g/2\pi = 15$  MHz, and  $\Delta_c/2\pi = 100$  MHz. STIRAP and SATD results are shown with dashed and solid curves, respectively, with the same colors for each  $T_{2\phi}$  value. The gray shaded region is the same as defined in Fig. 4, but for  $g/2\pi = 15$  MHz.

[17,48–50] (see also Appendix D)

$$g_{ac}(t) = g \left[ \sin \theta(t) + \frac{\cos[\theta(t)]\ddot{\theta}(t)}{g^2 + \dot{\theta}(t)^2} \right], \quad (7)$$

$$g_{bc}(t) = g \left[ \cos \theta(t) - \frac{\sin[\theta(t)]\ddot{\theta}(t)}{g^2 + \dot{\theta}(t)^2} \right], \quad (8)$$

where the corrections depend on both the first  $\dot{\theta}(t)$  and second derivatives  $\ddot{\theta}(t)$  of the mixing angle (see Appendix D for a comparison of pulse shapes).

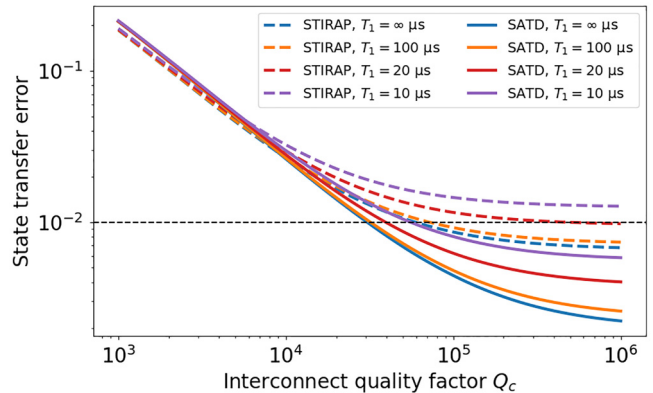


FIG. 6. Dependence of state transfer error on qubit/interconnect relaxation: comparing STIRAP (dashed) and SATD (solid) results as a function of interconnect quality factor  $Q_c$  for various qubit lifetimes of  $T_{1,a} = T_{1,b} \in \{\infty, 100, 20, 10\}$   $\mu$ s, fixed  $T_{2\phi,a} = T_{2\phi,b} = 10$   $\mu$ s, and  $g/2\pi = 15$  MHz. Operation times for STIRAP (SATD) are picked according to the corresponding minimum in Fig. 5 as  $\tau_p = 65$  ns ( $\tau_p = 44$  ns).

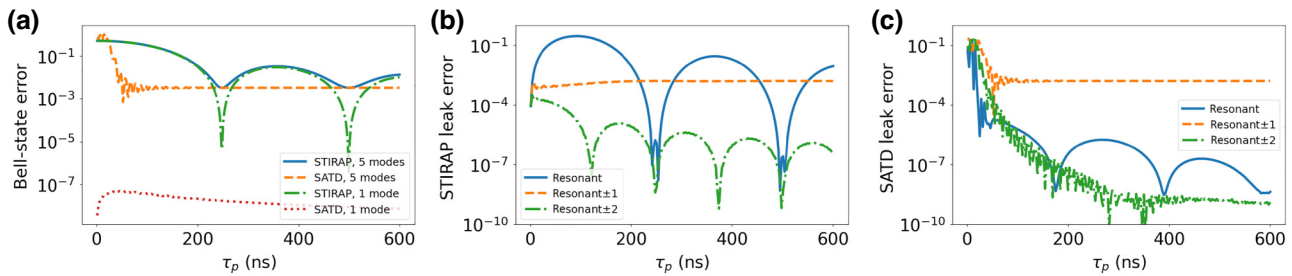


FIG. 7. Comparison of the performance and leakage breakdown for Bell-state generation of STIRAP versus SATD. This figure has the same format as Fig. 3 except for a weaker qubit-interconnect  $g/2\pi = 4$  MHz [approximately optimal based on Fig. 2(b)]. The enhanced population of the odd interconnect modes is caused by the even/odd coupling sign, and it is far more detrimental to Bell-state generation. Leakage to interconnect modes that are symmetrically above and below the center frequency is identical and is shown via a single curve.

In the following, we characterize and compare the performance of the regular STIRAP and SATD protocols and dissect various favorable aspects of SATD usage in the context of multimode interconnects for quantum state transfer and Bell-state generation. Some advantages of the SATD protocol, as compared with STIRAP, can be summarized as follows:

(i) The speed of standard STIRAP is limited by the dark  $\rightarrow$  bright transitions, whose effective transition frequency is equivalent to the resonant interaction rate  $g$  (Appendix B). SATD, however, removes the dark  $\rightarrow$  bright leakage and allows for faster operations whose speed limit is set by leakage to the adjacent interconnect modes (Appendix D, Figs. 3 and 7).

(ii) One crucial practical consequence of (i) is the SATD robustness to qubit-interconnect interaction  $g$  and the possibility of performing fast high-fidelity operations even with weak interactions (see Fig. 4 and Appendix D for  $g$ -robustness speed limits).

(iii) SATD provides a more pronounced speedup over STIRAP for Bell-state generation. This is because Bell-state generation is more sensitive to the even/odd sign dependence of the interaction when compared with state transfer, and it requires a weaker coupling to mitigate adiabatic overlap with the odd modes (Appendix C and Fig. 7).

(iv) We observe improved sensitivity of the SATD protocol error, as compared with STIRAP, with respect to qubit relaxation and pure dephasing (Figs. 5–6 and 8–9).

### A. Quantum state transfer

We begin by analyzing the performance of SATD for quantum state transfer. Figure 3 shows a comparison and breakdown of the quantum state transfer error between the regular STIRAP and SATD protocols. To emphasize the corrections provided by adopting the single-mode SATD solutions in this multimode setting, here,

we present the results considering both single- and five-interconnect modes and for zero qubit pure dephasing and qubit/interconnect relaxation. Figure 3(a) shows that for regular STIRAP, the single- and five-mode curves agree, indicating that state-transfer error is limited *mainly* by leakage to the resonant interconnect mode. The single-mode SATD simulation confirms the elimination of this leakage down to numerical error, as expected. Applying the single-mode SATD solutions (7) and (8) in the multimode setting is still advantageous in terms of operation time (orange curve). Figures 3(b) and 3(c) show the breakdown of final-time leakage to individual interconnect modes, where for SATD the error is mainly limited by leakage to the adjacent interconnect modes at shorter times.

To demonstrate the robustness of the SATD protocol with respect to  $g$  and the interplay with FSR  $\Delta_c$ ,

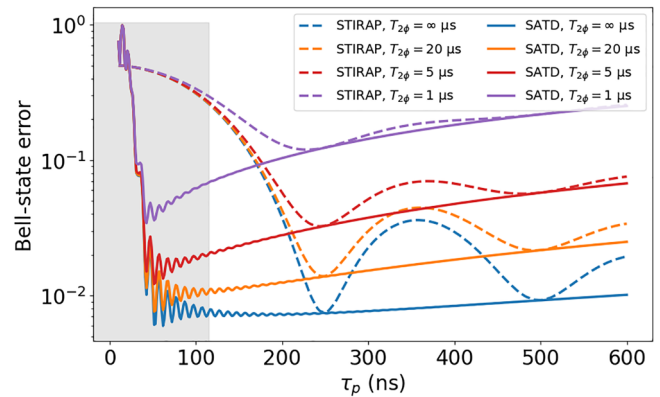


FIG. 8. Dependence of Bell-state error on pure dephasing: comparing STIRAP and SATD as a function of  $\tau_p$  for various dephasing times  $T_{2\phi,a} = T_{2\phi,a} \in \{\infty, 20, 5, 1\}$   $\mu$ s. Other parameters are set as  $T_{1a} = T_{1b} = 100$   $\mu$ s,  $Q_c = 10^5$ ,  $g/2\pi = 4$  MHz, and  $\Delta_c/2\pi = 100$  MHz. STIRAP and SATD results are shown with dashed and solid curves with the same colors for each  $T_{2\phi}$  value. The gray shaded region is the same as defined in Fig. 4.

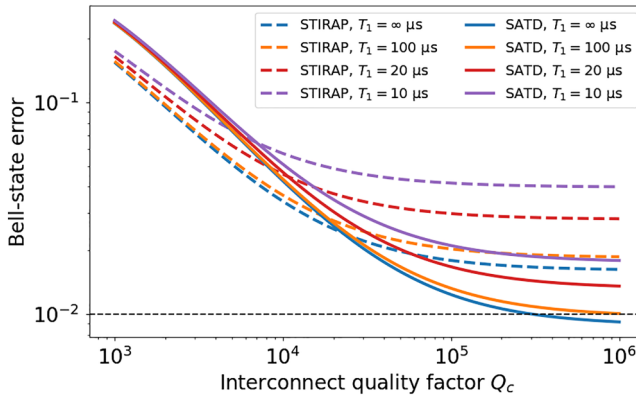


FIG. 9. Dependence of Bell-state error on qubit/interconnect relaxation: comparing STIRAP (dashed) and SATD (solid) results as a function of interconnect quality factor  $Q_c$  for various qubit lifetimes of  $T_{1a} = T_{1b} \in \{\infty, 100, 20, 10\}$   $\mu\text{s}$ , fixed  $T_{2\phi,a} = T_{2\phi,b} = 10$   $\mu\text{s}$ , and  $g/2\pi = 4$  MHz. Operation times for STIRAP (SATD) are picked according to Fig. 8 as  $\tau_p = 250$  ns ( $\tau_p = 100$  ns).

we compare the performance of STIRAP and SATD for weaker-than-optimal couplings in Fig. 4. Comparing the state transfer error for fixed  $\Delta_c/2\pi = 100$  MHz and two choices of  $g/2\pi = 4.0$  and  $8.0$  MHz in Fig. 4(a) shows the operation time of standard STIRAP to be inversely proportional to  $g$ , where we find optimal errors of approximately  $0.009$  and  $0.017$  at  $120$  and  $241$  ns (double), respectively. On the other hand, for SATD, the two coupling choices provide a comparable errors, showing that it is robust to variations in  $g$  and  $\tau_p$  according to a speed limit set by  $g\tau_p \geq 0.928\pi$  (see Appendix D). This feature of SATD is very beneficial, as it allows high-fidelity fast operations to be run even at weak coupling rates. In Fig. 4(b), we show a similar comparison but for a fixed weak  $g/2\pi = 4.0$  MHz and two choices of interconnect FSR (which is inversely proportional to length),  $\Delta_c/2\pi = 100$  and  $400$  MHz. This emphasizes the distinct error behavior: for STIRAP, the error is mostly dependent on the choice of  $g$ , while for SATD it is limited by the FSR/length of the interconnect at fast operation times.

We also assess the improvement achieved by SATD, as compared with STIRAP, in error sensitivity to pure dephasing and relaxation of qubits in Figs. 5 and 6, with the approximately optimal  $g/2\pi = 15$  MHz for state transfer [Fig. 2(a)]. We find that the incoherent errors due to dephasing and relaxation are approximately additive. Figure 5 shows the state transfer error as a function of  $\tau_p$  for various  $T_{2\phi} \in [\infty, 1]$   $\mu\text{s}$ . First, due to the expedited transfer, the pure dephasing error  $\Delta E_{\text{deph}}(T_{2\phi}) \equiv E_{T_{2\phi}} - E_{T_{2\phi} \rightarrow \infty}$  for SATD is substantially reduced, where at  $\tau_p \approx 44$  ns we find  $\Delta E_{\text{deph}}^{\text{SATD}}(1 \mu\text{s}) \approx 1.6 \times 10^{-2}$ . Moreover, at a longer (standard) STIRAP time of  $\tau_p = 4\pi/g \approx 130$  ns,

SATD demonstrates a substantial improvement in dephasing error as  $\Delta E_{\text{deph}}^{\text{SATD}}(1 \mu\text{s}) \approx 2.2 \times 10^{-2}$  compared with  $\Delta E_{\text{deph}}^{\text{STIRAP}}(1 \mu\text{s}) \approx 6.0 \times 10^{-2}$ . Furthermore, Fig. 6 shows the error as a function of the quality factor  $Q_c \in \{10^3, 10^6\}$  for various relaxation times  $T_1 \in \{\infty, 10\}$   $\mu\text{s}$ . We observe that SATD offers a substantial improvement in sensitivity with respect to qubit  $T_1$  as  $\Delta E_{\text{q-rel}}^{\text{SATD}}(10 \mu\text{s}) \approx 3.6 \times 10^{-3}$  compared with  $\Delta E_{\text{q-rel}}^{\text{STIRAP}}(10 \mu\text{s}) \approx 6.0 \times 10^{-3}$  at sufficiently large  $Q_c$ .

## B. Bell-state generation

We next discuss the advantages of the SATD protocol for Bell-state (entanglement) generation. The trade-offs/benefits demonstrated in Sec. IV A for state transfer also apply to Bell-state generation. In addition, Bell state generation is more affected by the even/odd sign of interaction, and hence requires a weaker qubit-interconnect  $g$  as found in Fig. 2(b). The use of regular STIRAP, however, means that the operation time will be set by  $g$  and hence will become relatively slow; therefore, SATD, whose speed is mostly limited by  $\Delta_c$ , provides a larger speedup for Bell-state generation compared with state transfer.

Figure 7 shows a comparison between STIRAP and SATD, similar to that in Fig. 3 with zero relaxation and dephasing, for Bell-state generation. Figure 7(a) shows that the SATD solution cancels out the resonant nonadiabatic error entirely; the five-mode simulation, however, manifests a constant floor for the error at sufficiently long times independent of  $\tau_p$ . The breakdown of interconnect mode populations in Figs. 7(b) and 7(c) reveals the source of this error as loss of qubit population to the odd modes, which is almost equal between STIRAP and SATD. We find that this adiabatic overlap of the supposedly dark state with the odd modes scales approximately as  $(g/\Delta_c)^2$ . Here, we have picked a weak coupling of  $g/2\pi = 4$  MHz, which suppresses the overlap error down to  $3.2 \times 10^{-3}$ . In this regime, SATD gives a noticeable speedup, where the fastest operation times for STIRAP and SATD are approximately  $250$  and  $100$  ns, respectively. Furthermore, Figs. 8 and 9 characterize the sensitivity of the Bell-state generation error to pure dephasing and qubit/interconnect relaxation in a similar format as in Figs. 5 and 6 but for  $g/2\pi = 4$  MHz. In this weak-coupling limit, SATD leads to a noticeable reduction in error sensitivity to pure dephasing, where at  $\tau_p \approx 100$  ns we find  $\Delta E_{\text{deph}}^{\text{SATD}}(1 \mu\text{s}) = 5.11 \times 10^{-2}$ , compared with  $\Delta E_{\text{deph}}^{\text{STIRAP}}(1 \mu\text{s}) = 1.164 \times 10^{-1}$  at  $\tau_p \approx 250$  ns. Moreover, based on Fig. 9, SATD achieves improved error sensitivity with respect to  $T_1$ , where  $\Delta E_{\text{q-rel}}^{\text{SATD}}(10 \mu\text{s}) \approx 8.7 \times 10^{-3}$  compared with  $\Delta E_{\text{q-rel}}^{\text{STIRAP}}(10 \mu\text{s}) \approx 2.37 \times 10^{-2}$  at sufficiently large  $Q_c$ .

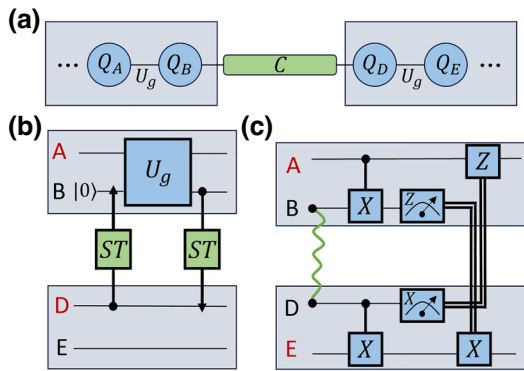


FIG. 10. Examples of remote *indirect* two-qubit gate schemes. (a) Schematics of two quantum modules coupled via an interconnect. (b) A protocol that combines an arbitrary local two-qubit gate  $U_g$  between qubits A and B with two remote quantum state transfers between qubits B and D to ideally achieve the same, but with a remote gate  $U_g$  between qubits A and D. A similar two-qubit gate can be implemented between qubits B and E. (c) The CNOT gate teleportation protocol [15,16,61,62] requires an initial Bell state, two local CNOT gates, and two midcircuit measurements and feedforward operations to achieve a remote CNOT between qubits A and E. The default entangled state in this protocol is  $|\Phi_+\rangle \equiv (1/\sqrt{2})(|00\rangle + |11\rangle)$  (squiggly line), which is equivalent to the state produced by STIRAP/SATD up to local X and Z operations (not shown for brevity).

### C. Practical impacts of SATD on indirect remote two-qubit gate schemes

To put the SATD improvements into perspective, we revisit the two indirect two-qubit gate schemes shown in Fig. 10. Imagine two QPUs with qubits A and B on the left, and D and E on the right. In each unit, we can perform a native two-qubit gate  $\hat{U}_g$ ; however, we assume that between the interface qubits B and D across the interconnect C, we can only perform quantum state transfer or generate entanglement.

The first scheme in Fig. 10(b) allows the arbitrary native two-qubit gate  $\hat{U}_g$  to act between an interface qubit and the qubit adjacent to the interface qubit on the other side. For instance, to perform a remote gate between qubits A and D we need to: (i) initialize qubit B in the ground state  $|0\rangle$ , (ii) transfer the state of D to B, (iii) perform the local native gate  $\hat{U}_g$ , and (iv) transfer the state of B back to D. In other words,  $\hat{U}_{g,AD} = \hat{S}T_{B \rightarrow D} \hat{U}_{g,AB} \hat{S}T_{D \rightarrow B}$ . A similar gate could be implemented between qubits B and E. Assuming sufficiently high fidelity for each individual operation, the average gate error [60] up to the leading order is roughly  $\bar{E}_{g,AD} \approx \bar{E}_{U_g} + 2\bar{E}_{ST}$ . Given the requirement for two state transfers, we expect the use of SATD to give noticeable improvement in both the gate speed and the average error. For instance, with  $g/2\pi \approx 15$  MHz, in Ref. [24] a 130-ns state transfer is calibrated using STIRAP, while

with SATD, we expect an  $\mathcal{O}(50)$ -ns transfer time for an FSR of  $\mathcal{O}(100)$  MHz.

Figure 10(c) shows the well-known controlled NOT (CNOT) teleportation scheme [15,16,61,62]. The protocol requires an initial entangled Bell pair between the interface qubits B and D, which can be prepared using STIRAP or SATD. Applying two local CNOT gates and two midcircuit measurements and feedforward operations across the interconnect yields an effective CNOT gate between the outer qubits A and E. We expect the fidelity of the protocol to be mainly limited by the relatively long midcircuit measurements and feedforward operations. The requirement for a weaker optimal  $g/2\pi \approx 4$  MHz, however, makes the use of SATD more crucial, and it can expedite the Bell generation considerably, e.g., from 250 ns down to  $\mathcal{O}(100)$  ns (see Fig. 8).

## V. CONCLUSION AND OUTLOOK

In this work, we promote the general application of shortcuts to adiabaticity methods [63–65], in particular SATD for STIRAP [17,48–50], in improving remote entanglement generation and quantum state transfer in multimode interconnects. Our results have applications to both long-range QPU-QPU connections and potential on-chip connections. In addition to introducing new leakage and decay channels, we find that the multimode nature of an interconnect violates the dark-state symmetry required for adiabatic passage by an adiabatic overlap error with the odd modes that grows as  $(g/\Delta_c)^2$ , which impacts entanglement generation more strongly. This observation makes SATD a great fit in this multimode context because its robustness against  $g$  allows for fast quantum operations at a sufficiently weak  $g$ , and it also suppresses the overlap error. For a meter-long interconnect with an FSR of 100 MHz, we can calibrate an  $\mathcal{O}(50)$  ns quantum state transfer and a Bell state with subpercent error.

We find the single-interconnect-mode SATD solutions [17,48–50] to work approximately as intended in the weak- $g$  limit such that only leakage in the resonant subspace (dark-bright transitions) is canceled out, and the operation speed is limited by leakage to the adjacent modes, which is set by the interconnect FSR. A potential future research direction is expediting the operation even further by suppressing leakage to the off-resonant modes. One could ask whether precise or approximate SATD solutions exist in the multimode case, and whether they can be implemented via the same control knobs. Furthermore, the single-mode SATD solutions can potentially serve as reasonable initial guesses for numerical optimal control techniques [66,67] for further leakage improvement.

## ACKNOWLEDGMENTS

We appreciate helpful discussions with the IBM Quantum members Vikesh Siddhu, Theodore J. Yoder, Alireza

Seif, Luke C. G. Govia, Muir Kumph, Jerry M. Chow, and Jay M. Gambetta. The authors acknowledge the IBM Research Cognitive Computing Cluster (CCC) service for providing resources that have contributed to the research results reported within this paper.

## APPENDIX A: LINDBLAD SIMULATION

For our numerical modeling of STIRAP and SATD, we run Lindblad simulations with two qubits and a finite number of interconnect modes. The Hamiltonian can be approximately described as

$$\begin{aligned} \hat{H}_s(t) = & \sum_{q=a,b} \left[ \omega_q(t) \hat{q}^\dagger \hat{q} + \frac{1}{2} \alpha_q \hat{q}^\dagger \hat{q}^\dagger \hat{q} \hat{q} \right] + \sum_{n=n_c=-N}^N \omega_n c_n^\dagger \hat{c}_n \\ & + \sum_{n=n_c=-N}^N g_{an}(t) (\hat{a} \hat{c}_n^\dagger + \hat{a}^\dagger \hat{c}_n) \\ & + \sum_{n=n_c=-N}^N g_{bn}(t) (-1)^n (\hat{b} \hat{c}_n^\dagger + \hat{b}^\dagger \hat{c}_n), \end{aligned} \quad (\text{A1})$$

with  $\hat{a}$ ,  $\hat{b}$ , and  $\hat{c}_n$  denoting the qubits and the  $n$ th interconnect modes, respectively;  $\omega$ ,  $\alpha$ , and  $g$  represent the mode frequency, anharmonicity, and exchange interaction, respectively. The multimode interconnect is modeled as a set of  $2N + 1$  linear quantum harmonic oscillators as  $\omega_n = \omega_{n_c} + n\Delta_c$  with the center frequency  $\omega_{n_c}$  and FSR  $\Delta_c$ .

We account for various incoherent error sources such as qubit relaxation, cable relaxation, and qubit pure dephasing, by numerically solving the following Lindblad equation for the system density matrix  $\hat{\rho}_s(t)$ :

$$\begin{aligned} \dot{\hat{\rho}}_s(t) = & -i[\hat{H}_s(t), \hat{\rho}_s(t)] + \sum_{q=a,b} \frac{1}{T_{1q}} \mathcal{D}[\hat{q}] \hat{\rho}_s(t) \\ & + \sum_{q=a,b} \frac{2}{T_{2\phi,q}} \mathcal{D}[\hat{q}^\dagger \hat{q}] \hat{\rho}_s(t) + \sum_n \kappa_n \mathcal{D}[\hat{c}_n] \hat{\rho}_s(t), \end{aligned} \quad (\text{A2})$$

where  $T_{1q}$  and  $T_{2\phi,q}$  are the relaxation and pure dephasing times for qubit  $q = a, b$ , respectively, and  $\kappa_n$  is the decay rate of the  $n$ th interconnect mode. Furthermore,  $\mathcal{D}[\hat{C}] \hat{\rho}_s \equiv \hat{C} \hat{\rho}_s \hat{C}^\dagger - (1/2)\{\hat{C}^\dagger \hat{C}, \hat{\rho}_s\}$  is the dissipator for the collapse operator  $\hat{C}$ .

A few remarks are in order. First, the qubit Hamiltonian is expressed as a multi-level Kerr oscillator. For the purpose of modeling state transfer and Bell-state generation, however, the time evolution is fairly accurately described by the one-excitation subspace; therefore, the two-level approximation works well. Second, we have performed the rotating-wave approximation on the qubit-

interconnect interactions given the experimentally relevant realizations, where  $g_{qc}/2\pi \approx \mathcal{O}(10)$  MHz and  $\omega_q/2\pi \approx \mathcal{O}(5)$  GHz. Third, the qubit-interconnect interaction rates  $g_{qn}$  for  $q = a, b$  in principle depend on the mode number approximately as  $g_{qm}/g_{qn} \approx (\omega_m/\omega_n)^{1/2}$  [68–71]. For a long coupler, however, qubits are resonant with a high-order interconnect mode, making the modal dependence of the interaction less pronounced. Fourth, the phase factor  $(-1)^n$  for the qubit  $b$  interaction rate accounts for the opposite amplitude sign of even and odd spatial modes at the two ends of the interconnect.

For all results in the main text, we have accounted for five interconnect modes: one resonant with the qubits and two on each side. Even under a two-level approximation for the qubits and the modes, this constitutes a large density matrix of dimension  $128 \times 128$  ( $D = 2^7 = 128$ ). Figure 11(a) shows convergence tests of state transfer error with one, three, and five interconnect modes. Generally speaking, a stronger  $g$  leads to more pronounced multimode effects involving further detuned modes. Our choice of five interconnect modes is a balance between simulation precision and speed for  $g/2\pi$  of up to approximately 15 MHz used in the main text. Furthermore, since STIRAP is excitation preserving, higher-levels of the qubits would not impact the dynamics, as shown in Fig. 11(b).

Lastly, we note that our numerical simulation of the Lindblad dynamics (A1) and (A2) was performed using Qiskit Dynamics [72,73], along with standard PYTHON scientific-computing packages including NUMPY [74] and SCIPY [75]. We used the DOP853 ordinary differential equation solver with absolute and relative tolerances set to `atol=rtol=1e-10`. The simulations were parallelized over multiple CPU cores (up to 250) on IBM's Cognitive Computing Cluster.

## APPENDIX B: SINGLE-MODE STIRAP

Consider a resonant Lambda system with tunable interaction rates between the qubit states  $q = a, b$  and coupler state  $c$  as

$$\begin{aligned} \hat{H}_{\text{STRP}}(t) = & \begin{bmatrix} 0 & g_{ac}(t) & 0 \\ g_{ac}(t) & 0 & g_{bc}(t) \\ 0 & g_{bc}(t) & 0 \end{bmatrix} \\ = & \begin{bmatrix} 0 & g(t) \sin \theta(t) & 0 \\ g(t) \sin \theta(t) & 0 & g(t) \cos \theta(t) \\ 0 & g(t) \cos \theta(t) & 0 \end{bmatrix}, \end{aligned} \quad (\text{B1})$$

where in the second step we have re-expressed the interactions as  $g(t) \equiv \sqrt{g_{ac}^2(t) + g_{bc}^2(t)}$  and  $\tan \theta(t) \equiv g_{ac}(t)/g_{bc}(t)$ . This resonant  $\Lambda$  system contains two bright eigenstates and one dark instantaneous eigenstate, where dark refers to there being no overlap with the intermediate interconnect state. Explicitly, Hamiltonian (B1) can be

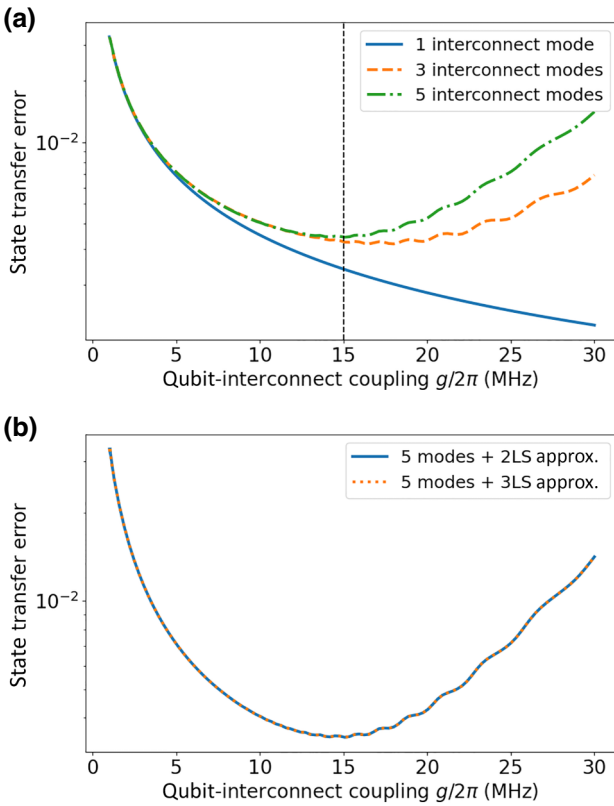


FIG. 11. Numerical convergence test. State transfer error for STIRAP (a) when including one, three, and five interconnect modes, and (b) when making two- or three-level approximations for the qubits. Parameters are set similar to those in Fig. 2(a) with  $Q_c = 10^5$ . The vertical dashed line in panel (a) shows the largest coupling used in our simulations.

diagonalized as

$$\hat{H}_{\text{INST}} \equiv \hat{U}_{\text{INST}} \hat{H}_{\text{STRP}} \hat{U}_{\text{INST}}^\dagger = \begin{bmatrix} +g(t) & 0 & 0 \\ 0 & 0 & 0 \\ 0 & 0 & -g(t) \end{bmatrix} \quad (\text{B2})$$

via the unitary transformation

$$\hat{U}_{\text{INST}} = \begin{bmatrix} \sin \theta(t)/\sqrt{2} & 1/\sqrt{2} & \cos \theta(t)/\sqrt{2} \\ \cos \theta(t) & 0 & -\sin \theta(t) \\ \sin \theta(t)/\sqrt{2} & -1/\sqrt{2} & \cos \theta(t)/\sqrt{2} \end{bmatrix}, \quad (\text{B3})$$

where the rows of Eq. (B3) represent the bright and dark eigenstates, having eigenenergies  $E_{B,\pm}(t) = \pm g(t)$  and  $E_D(t) = 0$ , respectively.

Under STIRAP, we adiabatically evolve the dark state  $|D(t)\rangle = \cos \theta(t) |1_a 0_c 0_b\rangle - \sin \theta(t) |0_a 0_c 1_b\rangle$  of the system by sweeping the angle  $\theta(t)$ . Starting with  $\theta(0) = 0$ , we can create a Bell state or perform state transfer at final

angle  $\theta(\tau_p) = \pi/4$  and  $\theta(\tau_p) = \pi/2$ , respectively. Common control pulse shapes are

$$g_{ac}(t) = g \sin \theta(t), \quad (\text{B4})$$

$$g_{bc}(t) = g \cos \theta(t), \quad (\text{B5})$$

$$\theta(t) = \theta_p \frac{t}{\tau_p}. \quad (\text{B6})$$

which keeps the bright-dark transition frequency constant in time equal to  $g$ . The nonadiabatic error of STIRAP is explicitly found by the time-dependent transformation of the Schrödinger equation in the instantaneous frame as

$$\begin{aligned} \hat{H}_{\text{NAD}} &\equiv i \dot{\hat{U}}_{\text{INST}} \hat{U}_{\text{INST}}^\dagger \\ &= \begin{bmatrix} 0 & +i\dot{\theta}(t) & 0 \\ -i\dot{\theta}(t) & 0 & -i\dot{\theta}(t) \\ 0 & +i\dot{\theta}(t) & 0 \end{bmatrix}, \end{aligned} \quad (\text{B7})$$

which is responsible for dark-bright state transitions whose strength is determined by the STIRAP speed  $\dot{\theta}(t)$ .

We can derive leading-order expressions for the dark-bright transitions using Magnus expansion [76–78]. Employing the control pulse shapes (B4) and (B5), and in the frame rotating with the instantaneous Hamiltonian (B2), the nonadiabatic Hamiltonian is transformed to

$$\begin{aligned} \hat{H}_{\text{NAD}}(t) &= e^{i\hat{H}_{\text{INST}} t} \hat{H}_{\text{NAD}}(0) e^{-i\hat{H}_{\text{INST}} t} \\ &= \begin{bmatrix} 0 & +i\dot{\theta}(t)e^{-igt} & 0 \\ -i\dot{\theta}(t)e^{+igt} & 0 & -i\dot{\theta}(t)e^{+igt} \\ 0 & +i\dot{\theta}(t)e^{-igt} & 0 \end{bmatrix}. \end{aligned} \quad (\text{B8})$$

Up to the lowest order, the Magnus generator and the time-evolution operator are found as [78]

$$\hat{U}_{\text{NAD}}(t, 0) = \hat{I} - i \hat{G}_1(t, 0) + \mathcal{O}(\hat{H}_{\text{NAD}}^2(t)), \quad (\text{B9})$$

$$\hat{G}_1(t, 0) \equiv \int_0^t dt' \hat{H}_{\text{NAD}}(t'). \quad (\text{B10})$$

We finally compute the dark-bright transition probability up to the leading order as

$$\begin{aligned} P_{D \rightarrow B_\pm}(t, 0) &\equiv \left| \langle B_\pm(t) | \hat{U}_{\text{NAD}}(t, 0) | D(0) \rangle \right|^2 \\ &\approx \left| \int_0^t dt' \dot{\theta}(t') e^{\mp igt'} \right|^2 + \mathcal{O}(\hat{H}_{\text{NAD}}^2(t)). \end{aligned} \quad (\text{B11})$$

Based on Eq. (B11), for constant  $\dot{\theta}(t) = \theta_p/\tau_p$ , this leakage can be minimized if the operation time satisfies  $g\tau_p = 2n\pi$  for  $n \in \mathbb{N}$ , explaining the regular STIRAP lobes as, e.g., in Fig. 3(a).

## APPENDIX C: STIRAP CONSIDERATIONS FOR A MULTIMODE INTERCONNECT

In a multimode setting, where  $g$  is a non-negligible fraction of the interconnect's FSR  $\Delta_c$ , the off-resonant modes have a detrimental effect on the STIRAP protocol. Here, we provide a simplified argument on why using STIRAP for entanglement generation is more prone to multimode error compared with state transfer.

Note the qubits also form off-resonant Lambda systems with the adjacent interconnect modes. To study the role of off-resonant modes, and the even-odd sign-dependent interactions, consider the simplest multimode extension of Eq. (B1) as

$$\hat{H}_{\text{STRP}}^{\text{MM}}(t) = \begin{bmatrix} 0 & g_{ac}(t) & g_{ac}(t) & g_{ac}(t) & 0 \\ g_{ac}(t) & -\Delta_c & 0 & 0 & -g_{bc}(t) \\ g_{ac}(t) & 0 & 0 & 0 & g_{bc}(t) \\ g_{ac}(t) & 0 & 0 & \Delta_c & -g_{bc}(t) \\ 0 & -g_{bc}(t) & g_{bc}(t) & -g_{bc}(t) & 0 \end{bmatrix}, \quad (\text{C1})$$

where we add two adjacent interconnect modes with detunings  $\pm\Delta_c$ .

Due to the sign-dependent interactions, Hamiltonian (C1) only supports a pseudo-dark eigenstate of the form

$$|D_{\text{pseudo}}(t)\rangle \propto \begin{bmatrix} \cos[\theta(t)] \\ \frac{g(t)}{\Delta_c} \sin[2\theta(t)] \\ 0 \\ -\frac{g(t)}{\Delta_c} \sin[2\theta(t)] \\ -\sin[\theta(t)] \end{bmatrix}, \quad (\text{C2})$$

where  $g(t) \equiv \sqrt{g_{ac}^2(t) + g_{bc}^2(t)}$  and  $\tan \theta(t) \equiv g_{ac}(t)/g_{bc}(t)$ .

According to Eq. (C2), for the case of alternating interaction sign, the pseudo dark eigenstate has a nonzero overlap of magnitude  $|[g(t)/\Delta_c] \sin[2\theta(t)]|$  with the one-excitation subspace of the odd interconnect modes. For a hypothetical case of same-sign interaction, however, we find that the original dark state is supported with zero overlap with all interconnect modes. First, we emphasize that this unwanted overlap is an *adiabatic* error, which is independent of the STIRAP speed  $\dot{\theta}(t)$ , and it can only be mitigated by a weaker interaction  $g$ . Second, when sweeping the mixing angle from  $\theta(0) = 0$  to  $\theta(\tau_p) = \pi/2$  for state transfer, the unwanted end overlap is zero given that  $\sin[2\theta(\tau_p)] = \sin(\pi) = 0$ ; however, this is not the case for arbitrary entanglement generation and Bell-state generation with  $\theta(\tau_p) = \pi/4$  in particular, making it more susceptible to such an adiabatic error.

## APPENDIX D: SATD CORRECTION FOR STIRAP

Here, we revisit the SATD solutions for the STIRAP problem [17,48–50]. Under the SATD method, we actively

cancel out the nonadiabatic contribution by (i) correcting the controls and (ii) dressing the adiabatic evolution path. Here, we review the derivation of a special SATD solution in which both the control and the dressing is along the  $x$  direction:

$$\hat{H}_{\text{CTRL}}(t) \equiv \hat{U}_{\text{INST}}^\dagger(t) \left[ h_x(t) \hat{M}_x \right] \hat{U}_{\text{INST}}(t), \quad (\text{D1})$$

$$\hat{V}(t) \equiv \hat{R}_x[\mu(t)] = \exp[i\mu(t)\hat{M}_x], \quad (\text{D2})$$

where  $h_x(t)$  and  $\mu(t)$  are the  $x$  control amplitude and  $x$  dressing angle, respectively (to be determined), and  $\hat{M}_k$  for  $k = x, y, z$  is the spin-1 operator.

We then solve for  $h_x(t)$  and  $\mu(t)$  such that in the frame dressed by  $\hat{V}(t)$ , given by

$$\begin{aligned} \hat{H}_{\text{DRS}}(t) \equiv & \hat{V}(t) \left[ g \hat{M}_z(t) + \dot{\theta}(t) \hat{M}_y(t) + h_x(t) \hat{M}_x(t) \right] \hat{V}^\dagger(t) \\ & + i \dot{\hat{V}}(t) \hat{V}^\dagger(t), \end{aligned} \quad (\text{D3})$$

the off-diagonal nonadiabatic transitions are canceled out at arbitrary time  $t$ . Enforcing the cancelation results in the following equations:

$$\tan \mu(t) = -\frac{\dot{\theta}(t)}{g}, \quad (\text{D4})$$

$$h_x(t) = \dot{\mu}(t), \quad (\text{D5})$$

with an explicit solution for  $h_x(t)$  as

$$h_x(t) = -\frac{g\ddot{\theta}(t)}{g^2 + \dot{\theta}(t)^2}. \quad (\text{D6})$$

Transforming the corrected control back to the lab frame according to Eq. (D1), one finds the SATD solutions as

$$g_{ac}(t) = g \left[ \underbrace{\sin \theta(t) + \frac{\cos[\theta(t)]\ddot{\theta}(t)}{g^2 + \dot{\theta}(t)^2}}_{\text{SATD correction}} \right], \quad (\text{D7})$$

$$g_{bc}(t) = g \left[ \underbrace{\cos \theta(t) - \frac{\sin[\theta(t)]\ddot{\theta}(t)}{g^2 + \dot{\theta}(t)^2}}_{\text{SATD correction}} \right]. \quad (\text{D8})$$

To ensure that the initial and final points of the adiabatic evolution remain unchanged, we further enforce  $\dot{\theta}(t)|_{t=0,\tau_p} = \ddot{\theta}(t)|_{t=0,\tau_p} = 0$ , in addition to  $\theta(0) = 0$  and

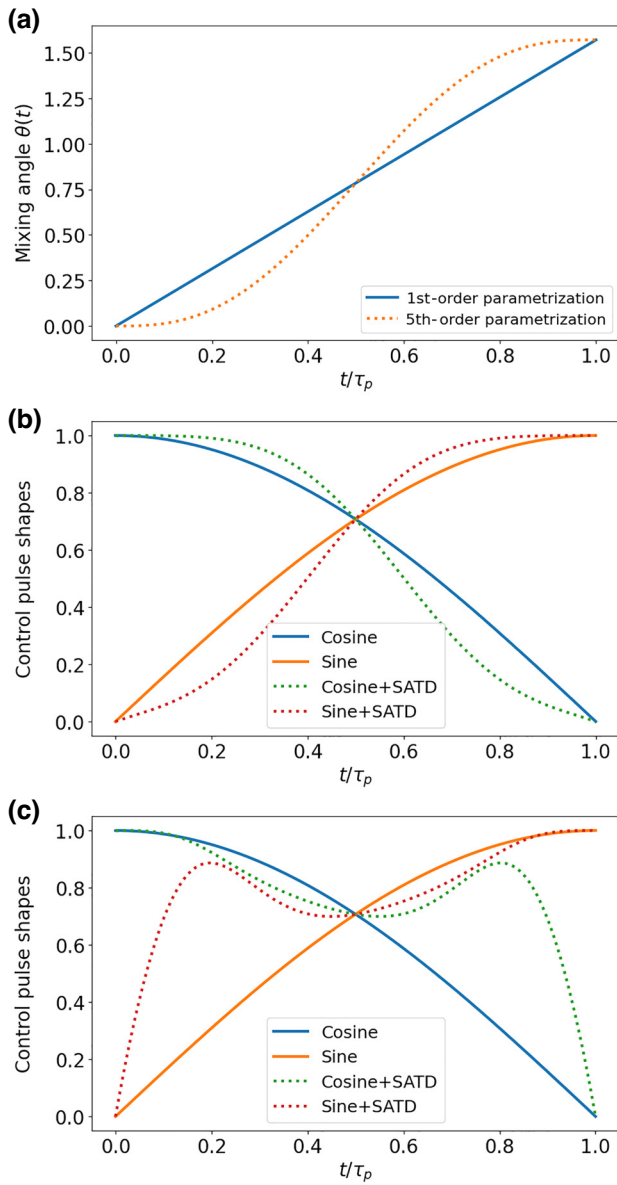


FIG. 12. STIRAP and SATD mixing angles and corresponding pulse shapes. (a) First-order (STIRAP) and fifth-order (SATD) polynomial parametrization of mixing angle as in Eqs. (B6) and (D9) with  $\theta_p = \pi/2$ . (b),(c) Corresponding STIRAP and SATD pulse shapes, given in Eqs. (B4), (B5), (D7), and (D8) for (b)  $g\tau_p = 4\pi$  and (c)  $g\tau_p = \pi$ .

$\theta(\tau_p) = \theta_p$ . The lowest-order polynomial satisfying these conditions is then found as

$$\theta^{(5)}(t) = \theta_p \left[ 6 \left( \frac{t}{\tau_p} \right)^5 - 15 \left( \frac{t}{\tau_p} \right)^4 + 10 \left( \frac{t}{\tau_p} \right)^3 \right]. \quad (\text{D9})$$

Lastly, we comment on the relation between  $g$  and  $\tau_p$  for the SATD solutions (D7) and (D8). Note that for STIRAP, the maximum pulse amplitude is set directly

by  $g$  because  $|\sin(\theta(t))| \leq 1$  and  $|\cos(\theta(t))| \leq 1$ . To minimize leakage in STIRAP, the operation is calibrated at  $g\tau_p = 2n\pi$  as described in Appendix B, with  $g\tau_p = 4\pi$  as a common choice. For SATD, however, the derivative corrections can grow in magnitude at sufficiently short  $\tau_p$ , where we find that  $|g_{ac}(t)/g| \leq 1$  and  $|g_{bc}(t)/g| \leq 1$  for operation times as fast as  $g\tau_p \gtrsim 0.928\pi$ . Below this limit, i.e.,  $g\tau_p < 0.928\pi$ , the SATD implementation requires a larger-than- $g$  maximum pulse amplitude for an exact leakage cancelation. This is a practical consideration, as such a larger interaction needs to be supported by the underlying hardware. In summary, with a fixed allowed maximum  $g(t)$ , SATD provides an approximate  $4\times$  speedup with respect to the standard STIRAP calibration ( $2\times$  speed-up with respect to the  $g\tau_p = 2\pi$  choice).

Figure 12 shows a comparison between the modified SATD control pulse shapes (D7)–(D9) and the standard STIRAP control in Eqs. (B4)–(B6), comparing the standard choice  $g\tau_p = 4\pi$  and the borderline choice of  $g\tau_p = \pi$ . Note that for  $g\tau_p = \pi$ , the derivative corrections are non-negligible and lead to nontrivial control shapes.

- [1] Simon J. Devitt, Austin G. Fowler, Ashley M. Stephens, Andrew D. Greentree, Lloyd C. L. Hollenberg, William J. Munro, and Kae Nemoto, Architectural design for a topological cluster state quantum computer, *New J. Phys.* **11**, 083032 (2009).
- [2] Christopher Monroe, Robert Raussendorf, Alex Ruthven, Kenneth R. Brown, Peter Maunz, L-M Duan, and Jungsang Kim, Large-scale modular quantum-computer architecture with atomic memory and photonic interconnects, *Phys. Rev. A* **89**, 022317 (2014).
- [3] Sergey Bravyi, Oliver Dial, Jay M. Gambetta, Darío Gil, and Zaira Nazario, The future of quantum computing with superconducting qubits, *J. Appl. Phys.* **132**, 160902 (2022).
- [4] Austin G. Fowler, Ashley M. Stephens, and Peter Groszkowski, High-threshold universal quantum computation on the surface code, *Phys. Rev. A* **80**, 052312 (2009).
- [5] Austin G. Fowler, Matteo Mariantoni, John M. Martinis, and Andrew N. Cleland, Surface codes: Towards practical large-scale quantum computation, *Phys. Rev. A* **86**, 032324 (2012).
- [6] Sergey Bravyi, Andrew W. Cross, Jay M. Gambetta, Dmitri Maslov, Patrick Rall, and Theodore J. Yoder, High-threshold and low-overhead fault-tolerant quantum memory, *Nature* **627**, 778 (2024).
- [7] Emanuel Knill and Raymond Laflamme, Theory of quantum error-correcting codes, *Phys. Rev. A* **55**, 900 (1997).
- [8] Daniel Gottesman, Ph.D. Thesis, California Institute of Technology, 1997.
- [9] Emanuel Knill, Raymond Laflamme, and Lorenza Viola, Theory of quantum error correction for general noise, *Phys. Rev. Lett.* **84**, 2525 (2000).
- [10] Daniel A. Lidar and Todd A. Brun, in *Quantum Error Correction* (Cambridge University Press, 2013),

- <https://www.cambridge.org/core/books/quantum-error-correction/B51E8333050A0F9A67363254DC1EA15A>.
- [11] Barbara M. Terhal, Quantum error correction for quantum memories, *Rev. Mod. Phys.* **87**, 307 (2015).
- [12] Alysson Gold, J. P. Paquette, Anna Stockklauser, Matthew J. Reagor, M. Sohaib Alam, Andrew Bestwick, Nicolas Didier, Ani Nersisyan, Feyza Oruc, Armin Razavi, *et al.*, Entanglement across separate silicon dies in a modular superconducting qubit device, *npj Quantum Inf.* **7**, 142 (2021).
- [13] C. R. Conner, A. Bienfait, H.-S. Chang, M.-H. Chou, É. Dumur, J. Grebel, G. A. Peairs, R. G. Povey, H. Yan, Y. P. Zhong, *et al.*, Superconducting qubits in a flip-chip architecture, *Appl. Phys. Lett.* **118**, 232602 (2021).
- [14] Daniel Gottesman and Isaac L. Chuang, Demonstrating the viability of universal quantum computation using teleportation and single-qubit operations, *Nature* **402**, 390 (1999).
- [15] Jens Eisert, Kurt Jacobs, Polykarpos Papadopoulos, and Martin B. Plenio, Optimal local implementation of nonlocal quantum gates, *Phys. Rev. A* **62**, 052317 (2000).
- [16] Yun-Feng Huang, Xi-Feng Ren, Yong-Sheng Zhang, Lu-Ming Duan, and Guang-Can Guo, Experimental teleportation of a quantum controlled-not gate, *Phys. Rev. Lett.* **93**, 240501 (2004).
- [17] Alexandre Baksic, Hugo Ribeiro, and Aashish A. Clerk, Speeding up adiabatic quantum state transfer by using dressed states, *Phys. Rev. Lett.* **116**, 230503 (2016).
- [18] Philipp Kurpiers, Paul Magnard, Theo Walter, Baptiste Royer, Marek Pechal, Johannes Heinsoo, Yves Salathé, Abdulkadir Akin, Simon Storz, J-C Besse, *et al.*, Deterministic quantum state transfer and remote entanglement using microwave photons, *Nature* **558**, 264 (2018).
- [19] Christopher J. Axline, Luke D. Burkhardt, Wolfgang Pfaff, Mengzhen Zhang, Kevin Chou, Philippe Campagne-Ibarcq, Philip Reinhold, Luigi Frunzio, S. M. Girvin, Liang Jiang, *et al.*, On-demand quantum state transfer and entanglement between remote microwave cavity memories, *Nat. Phys.* **14**, 705 (2018).
- [20] P. Campagne-Ibarcq, E. Zalys-Geller, A. Narla, S. Shankar, P. Reinhold, L. Burkhardt, C. Axline, W. Pfaff, L. Frunzio, R. J. Schoelkopf, *et al.*, Deterministic remote entanglement of superconducting circuits through microwave two-photon transitions, *Phys. Rev. Lett.* **120**, 200501 (2018).
- [21] N. Leung, Y. Lu, S. Chakram, R. K. Naik, N. Earnest, R. Ma, K. Jacobs, A. N. Cleland, and D. I. Schuster, Deterministic bidirectional communication and remote entanglement generation between superconducting qubits, *npj Quantum Inform.* **5**, 18 (2019).
- [22] Y. P. Zhong, H.-S. Chang, K. J. Satzinger, M.-H. Chou, Audrey Bienfait, C. R. Conner, É. Dumur, Joel Grebel, G. A. Peairs, R. G. Povey, *et al.*, Violating Bell's inequality with remotely connected superconducting qubits, *Nat. Phys.* **15**, 741 (2019).
- [23] Audrey Bienfait, Kevin J. Satzinger, Y. P. Zhong, H.-S. Chang, M.-H. Chou, Chris R. Conner, É. Dumur, Joel Grebel, Gregory A. Peairs, Rhys G. Povey, *et al.*, Phonon-mediated quantum state transfer and remote qubit entanglement, *Science* **364**, 368 (2019).
- [24] H.-S. Chang, Y. P. Zhong, Audrey Bienfait, M.-H. Chou, Christopher R. Conner, Étienne Dumur, Joel Grebel, Gregory A. Peairs, Rhys G. Povey, Kevin J. Satzinger, *et al.*, Remote entanglement via adiabatic passage using a tunably dissipative quantum communication system, *Phys. Rev. Lett.* **124**, 240502 (2020).
- [25] Youpeng Zhong, Hung-Shen Chang, Audrey Bienfait, Étienne Dumur, Ming-Han Chou, Christopher R. Conner, Joel Grebel, Rhys G. Povey, Haoxiong Yan, David I. Schuster, *et al.*, Deterministic multi-qubit entanglement in a quantum network, *Nature* **590**, 571 (2021).
- [26] Haoxiong Yan, Youpeng Zhong, Hung-Shen Chang, Audrey Bienfait, Ming-Han Chou, Christopher R. Conner, Étienne Dumur, Joel Grebel, Rhys G. Povey, and Andrew N. Cleland, Entanglement purification and protection in a superconducting quantum network, *Phys. Rev. Lett.* **128**, 080504 (2022).
- [27] Bharath Kannan, Aziza Almanakly, Youngkyu Sung, Agustin Di Paolo, David A. Rower, Jochen Braumüller, Alexander Melville, Bethany M. Niedzielski, Amir Karamlou, Kyle Serniak, *et al.*, On-demand directional microwave photon emission using waveguide quantum electrodynamics, *Nat. Phys.* **19**, 394 (2023).
- [28] Jingjing Niu, Libo Zhang, Yang Liu, Jiawei Qiu, Wenhui Huang, Jiaxiang Huang, Hao Jia, Jiawei Liu, Ziyu Tao, Weiwei Wei, *et al.*, Low-loss interconnects for modular superconducting quantum processors, *Nat. Electron.* **6**, 235 (2023).
- [29] Jiawei Qiu, Yang Liu, Jingjing Niu, Ling Hu, Yukai Wu, Libo Zhang, Wenhui Huang, Yuanzhen Chen, Jian Li, Song Liu, *et al.*, Deterministic quantum teleportation between distant superconducting chips, *ArXiv:2302.08756*.
- [30] Juan Ignacio Cirac, Peter Zoller, H. Jeff Kimble, and Hideo Mabuchi, Quantum state transfer and entanglement distribution among distant nodes in a quantum network, *Phys. Rev. Lett.* **78**, 3221 (1997).
- [31] A. David Boozer, Andreea Boca, Russell Miller, Tracy E. Northup, and H. Jeffrey Kimble, Reversible state transfer between light and a single trapped atom, *Phys. Rev. Lett.* **98**, 193601 (2007).
- [32] U. Gaubatz, P. Rudecki, S. Schiemann, and K. Bergmann, Population transfer between molecular vibrational levels by stimulated Raman scattering with partially overlapping laser fields. A new concept and experimental results, *J. Chem. Phys.* **92**, 5363 (1990).
- [33] Nikolay V. Vitanov, Andon A. Rangelov, Bruce W. Shore, and Klaas Bergmann, Stimulated Raman adiabatic passage in physics, chemistry, and beyond, *Rev. Mod. Phys.* **89**, 015006 (2017).
- [34] Klaas Bergmann, Hanns-Christoph Nägerl, Cristian Panda, Gerald Gabrielse, Eduard Miloglyadov, Martin Quack, Georg Seyfang, Gunther Wichmann, Silke Ospelkaus, Axel Kuhn, *et al.*, Roadmap on STIRAP applications, *J. Phys. B: At., Mol. Opt. Phys.* **52**, 202001 (2019).
- [35] Mustafa Demirplak and Stuart A. Rice, Adiabatic population transfer with control fields, *J. Phys. Chem. A* **107**, 9937 (2003).
- [36] Mustafa Demirplak and Stuart A. Rice, On the consistency, extremal, and global properties of counterdiabatic fields, *J. Chem. Phys.* **129**, 154111 (2008).
- [37] Michael Victor Berry, Transitionless quantum driving, *J. Phys. A: Math. Theor.* **42**, 365303 (2009).
- [38] Sara Ibáñez, Xi Chen, E. Torrontegui, Juan Gonzalo Muga, and Andreas Ruschhaupt, Multiple Schrödinger pictures

- and dynamics in shortcuts to adiabaticity, *Phys. Rev. Lett.* **109**, 100403 (2012).
- [39] Wen Zheng, Yu Zhang, Yuqian Dong, Jianwen Xu, Zhimin Wang, Xiaohan Wang, Yong Li, Dong Lan, Jie Zhao, Shaoxiong Li, *et al.*, Optimal control of stimulated Raman adiabatic passage in a superconducting qudit, *npj Quantum Inf.* **8**, 9 (2022).
- [40] F. Motzoi, J. M. Gambetta, P. Rebentrost, and F. K. Wilhelm, Simple pulses for elimination of leakage in weakly nonlinear qubits, *Phys. Rev. Lett.* **103**, 110501 (2009).
- [41] Jay M. Gambetta, F. Motzoi, S. T. Merkel, and Frank K. Wilhelm, Analytic control methods for high-fidelity unitary operations in a weakly nonlinear oscillator, *Phys. Rev. A* **83**, 012308 (2011).
- [42] Moein Malekakhlagh and Easwar Magesan, Mitigating off-resonant error in the cross-resonance gate, *Phys. Rev. A* **105**, 012602 (2022).
- [43] Boxi Li, Tommaso Calarco, and Felix Motzoi, Experimental error suppression in Cross-Resonance gates via multi-derivative pulse shaping, *npj Quantum Inf.* **10**, 66 (2024).
- [44] L. M. Garrido, Generalized adiabatic invariance, *J. Math. Phys.* **5**, 355 (1964).
- [45] Michael Victor Berry, Quantum phase corrections from adiabatic iteration, *Proc. R. Soc. Lond. A Math. Phys. Sci.* **414**, 31 (1987).
- [46] Michael Victor Berry, Histories of adiabatic quantum transitions, *Proc. R. Soc. Lond. A Math. Phys. Sci.* **429**, 61 (1990).
- [47] Brian B. Zhou, Alexandre Baksic, Hugo Ribeiro, Christopher G. Yale, F. Joseph Heremans, Paul C. Jerger, Adrian Auer, Guido Burkard, Aashish A. Clerk, and David D. Awschalom, Accelerated quantum control using superadiabatic dynamics in a solid-state lambda system, *Nat. Phys.* **13**, 330 (2017).
- [48] Hugo Ribeiro and Aashish A. Clerk, Accelerated adiabatic quantum gates: Optimizing speed versus robustness, *Phys. Rev. A* **100**, 032323 (2019).
- [49] F. Setiawan, Peter Groszkowski, Hugo Ribeiro, and Aashish A. Clerk, Analytic design of accelerated adiabatic gates in realistic qubits: General theory and applications to superconducting circuits, *PRX Quantum* **2**, 030306 (2021).
- [50] Fnu Setiawan, Peter Groszkowski, and Aashish A. Clerk, Fast and robust geometric two-qubit gates for superconducting qubits and beyond, *Phys. Rev. Appl.* **19**, 034071 (2023).
- [51] Vladimir E. Manucharyan, Jens Koch, Leonid I. Glazman, and Michel H. Devoret, Fluxonium: Single Cooper-pair circuit free of charge offsets, *Science* **326**, 113 (2009).
- [52] Neereja M. Sundaresan, Yanbing Liu, Darius Sadri, László J. Szócs, Devin L. Underwood, Moein Malekakhlagh, Hakan E. Türeci, and Andrew A. Houck, Beyond strong coupling in a multimode cavity, *Phys. Rev. X* **5**, 021035 (2015).
- [53] Rami Barends, Julian Kelly, Anthony Megrant, Daniel Sank, Evan Jeffrey, Yu Chen, Yi Yin, Ben Chiaro, Josh Mutus, Charles Neill, *et al.*, Coherent Josephson qubit suitable for scalable quantum integrated circuits, *Phys. Rev. Lett.* **111**, 080502 (2013).
- [54] Yu Chen, C. Neill, P. Roushan, N. Leung, M. Fang, R. Barends, J. Kelly, B. Campbell, Z. Chen, B. Chiaro, *et al.*, Qubit architecture with high coherence and fast tunable coupling, *Phys. Rev. Lett.* **113**, 220502 (2014).
- [55] Michael R. Geller, Emmanuel Donati, Yu Chen, Michael T. Fang, Nelson Leung, Charles Neill, Pedram Roushan, and John M. Martinis, Tunable coupler for superconducting Xmon qubits: Perturbative nonlinear model, *Phys. Rev. A* **92**, 012320 (2015).
- [56] Alessio Serafini, Stefano Mancini, and Sougato Bose, Distributed quantum computation via optical fibers, *Phys. Rev. Lett.* **96**, 010503 (2006).
- [57] B. Vogell, B. Vermersch, T. E. Northup, B. P. Lanyon, and C. A. Muschik, Deterministic quantum state transfer between remote qubits in cavities, *Quantum Sci. Technol.* **2**, 045003 (2017).
- [58] Janine Riedrich-Möller, Carsten Arend, Christoph Pauly, Frank Mücklich, Martin Fischer, Stefan Gsell, Matthias Schreck, and Christoph Becher, Deterministic coupling of a single silicon-vacancy color center to a photonic crystal cavity in diamond, *Nano Lett.* **14**, 5281 (2014).
- [59] Alp Sipahigil, Ruffin E. Evans, Denis D. Sukachev, Michael J. Burek, Johannes Borregaard, Mihir K. Bhaskar, Christian T. Nguyen, Jose L. Pacheco, Haig A. Atikian, Charles Meuwly, *et al.*, An integrated diamond nanophotonics platform for quantum-optical networks, *Science* **354**, 847 (2016).
- [60] Line Hjortshøj Pedersen, Niels Martin Møller, and Klaus Mølmer, Fidelity of quantum operations, *Phys. Lett. A* **367**, 47 (2007).
- [61] Kevin S. Chou, Jacob Z. Blumoff, Christopher S. Wang, Philip C. Reinhold, Christopher J. Axline, Yvonne Y. Gao, Luigi Frunzio, M. H. Devoret, Liang Jiang, and R. J. Schoelkopf, Deterministic teleportation of a quantum gate between two logical qubits, *Nature* **561**, 368 (2018).
- [62] Yong Wan, Daniel Kienzler, Stephen D. Erickson, Karl H. Mayer, Ting Rei Tan, Jenny J. Wu, Hilma M. Vasconcelos, Scott Glancy, Emanuel Knill, David J. Wineland, *et al.*, Quantum gate teleportation between separated qubits in a trapped-ion processor, *Science* **364**, 875 (2019).
- [63] Christopher Jarzynski, Generating shortcuts to adiabaticity in quantum and classical dynamics, *Phys. Rev. A* **88**, 040101 (2013).
- [64] Sebastian Deffner, Christopher Jarzynski, and Adolfo del Campo, Classical and quantum shortcuts to adiabaticity for scale-invariant driving, *Phys. Rev. X* **4**, 021013 (2014).
- [65] David Guéry-Odelin, Andreas Ruschhaupt, Anthony Kiely, Erik Torrontegui, Sofia Martínez-Garaot, and Juan Gonzalo Muga, Shortcuts to adiabaticity: Concepts, methods, and applications, *Rev. Mod. Phys.* **91**, 045001 (2019).
- [66] Navin Khaneja, Timo Reiss, Cindie Kehlet, Thomas Schulte-Herbrüggen, and Steffen J. Glaser, Optimal control of coupled spin dynamics: Design of NMR pulse sequences by gradient ascent algorithms, *J. Magn. Reson.* **172**, 296 (2005).
- [67] Christiane P. Koch, Ugo Boscain, Tommaso Calarco, Gunther Dirr, Stefan Filipp, Steffen J. Glaser, Ronnie Kosloff, Simone Montangero, Thomas Schulte-Herbrüggen, Dominique Sugny, *et al.*, Quantum optimal control in quantum technologies. Strategic report on current status, visions and goals for research in Europe, *EPJ Quantum Technol.* **9**, 19 (2022).

- [68] A. A. Houck, J. A. Schreier, B. R. Johnson, J. M. Chow, Jens Koch, J. M. Gambetta, D. I. Schuster, L. Frunzio, M. H. Devoret, S. M. Girvin, and R. J. Schoelkopf, Controlling the spontaneous emission of a superconducting transmon qubit, *Phys. Rev. Lett.* **101**, 080502 (2008).
- [69] Moein Malekakhlagh and Hakan E. Türeci, Origin and implications of an  $A^2$ -like contribution in the quantization of circuit-QED systems, *Phys. Rev. A* **93**, 012120 (2016).
- [70] Mario F. Gely, Adrian Parra-Rodriguez, Daniel Bothner, Ya M. Blanter, Sal J. Bosman, Enrique Solano, and Gary A. Steele, Convergence of the multimode quantum Rabi model of circuit quantum electrodynamics, *Phys. Rev. B* **95**, 245115 (2017).
- [71] Moein Malekakhlagh, Alexandru Petrescu, and Hakan E. Türeci, Cutoff-free circuit quantum electrodynamics, *Phys. Rev. Lett.* **119**, 073601 (2017).
- [72] Daniel Puzzuoli, Sophia Fuhui Lin, Moein Malekakhlagh, Emily Pritchett, Benjamin Rosand, and Christopher J. Wood, Algorithms for perturbative analysis and simulation of quantum dynamics, *J. Comput. Phys.* **489**, 112262 (2023).
- [73] Daniel Puzzuoli, Christopher J. Wood, Daniel J. Egger, Benjamin Rosand, and Kento Ueda, Qiskit Dynamics: A Python package for simulating the time dynamics of quantum systems, *J. Open Source Softw.* **8**, 5853 (2023).
- [74] Charles R. Harris, K. Jarrod Millman, Stéfan J. van der Walt, Ralf Gommers, Pauli Virtanen, David Cournapeau, Eric Wieser, Julian Taylor, Sebastian Berg, Nathaniel J. Smith, *et al.*, Array programming with NumPy, *Nature* **585**, 357 (2020).
- [75] Pauli Virtanen, Ralf Gommers, Travis E. Oliphant, Matt Haberland, Tyler Reddy, David Cournapeau, Evgueni Burovski, Pearu Peterson, Warren Weckesser, Jonathan Bright, *et al.*, SciPy 1.0: Fundamental algorithms for scientific computing in Python, *Nat. Methods.* **17**, 261 (2020).
- [76] Wilhelm Magnus, On the exponential solution of differential equations for a linear operator, *Commun. Pure Appl. Math.* **7**, 649 (1954).
- [77] Sergio Blanes, Fernando Casas, Jose-Angel Oteo, and José Ros, The Magnus expansion and some of its applications, *Phys. Rep.* **470**, 151 (2009).
- [78] Sergio Blanes, Fernando Casas, J. A. Oteo, and J. Ros, A pedagogical approach to the Magnus expansion, *Eur. J. Phys.* **31**, 907 (2010).